Shape of Asteroid 4769 Castalia (1989 PB) from Inversion of Radar Images

R. Scott Hudson and Steven J. Ostro.

Inversion of previously reported, delay-Doppler images of Castalia yields a 167-parameter, three-dimensional shape model that is bifurcated into two distinct, irregular, kilometer-sized lobes. The crevice that separates the lobes has an average depth of between 100 and 150 meters and is oriented roughly perpendicular to the asteroid's longest dimension. The constrained-least-squares reconstruction method introduced here can be used to determine the shape, spin vector, and radar scattering properties of any asteroid or comet for which delay-Doppler images provide sufficient signal-to-noise ratio, orientational coverage, and spatial resolution.

Radar observations can resolve Earth-crossing asteroids (ECAs) by measuring the distribution of echo power in time delay (range) and Doppler frequency: planes normal to the line of sight cut the target into range cells and, for a rigid target, planes parallel to both the line of sight and the target's apparent spin vector (1) cut the target into Doppler-frequency cells (2). Hence a delay-Doppler image can be visualized as the projection of the target's radar brightness onto a plane that contains the radar and is normal to the constant-delay, constant-Doppler lines. Each of those lines can intersect two or more noncontiguous points on the target, therefore, parts of the image can represent a many-to-one mapping, i.e., can be "north/south ambiguous." Moreover, the length equivalent of frequency in radar images is a function of the target's apparent spin vector, which may be poorly known. Accurate interpretation of ECA radar images consequently is nontrivial and usually requires multiple images that sample diverse orientations of the target.

Radar observations (9) of 4769 Castalia (formerly 1989 PB) yielded useful resolution and definition of this ECA's shape: a 2.5-h sequence of 64 images resolved the echo into a few dozen cells and revealed a bimodal distribution of echo power, Visual inspection along with analysis of the echoes' frame-t-frame bandwidth variation implied that Castalia is bifurcated into two kilometer-sized lobes apparently in contact with each other (9). In this Report wc describe an estimation of Castalia's three-dimensional shape from the delay-Doppler images.

Each of the 64 images in our data set (9) is the result of a 29-s integration and consists of an estimate of radar cross section σ as a function of time delay τ and Doppler frequency ν. The length equivalent of the 2-μs interval between time samples is 300 m. 'I'he length equivalent of the frequency-sampling interval, $\Delta\nu = 0.95$ Rz, is

$$\Delta x = \Delta\nu P\lambda/4\pi\cos\delta\ , \qquad (1)$$

with P the apparent rotation period, λ the wavelength (0.126 m), and δ the subradar latitude (measured from the asteroid's equatorial plane to the radar line of sight). For the estimated period, 4.07 ± 0.02 h, (9), the 64-frame sequence covers 220° of rotation phase ψ; each image spans $\Delta\psi = 0.7°$. Since the asteroid's position on the sky changed by less than 1° during the entire imaging sequence, the contribution of that angular motion to the apparent rotation is negligible. We therefore assume that δ was constant throughout the sequence. Our shape reconstruction treated both δ and P as free parameters.

We employed two shape models: a "one-component" model and a "two-component" model. The one-component model has a surface S defined by

$$S = \{\mathbf{r}\,|\mathbf{r} = r(\theta,\phi)[\sin\theta\cos\phi, \sin\theta\sin\phi, \cos\theta)\} \qquad (2)$$

for $0 \le \theta \le \pi, 0 \le \phi < 2\pi$, where

$$r(\theta,\phi) = \sum_{l=0}^{L}\left\{a_{l0}P_l^0(\cos\theta) + \sum_{m=1}^{l}[a_{lm}\cos(m\phi) + b_{lm}\sin(m\phi)]P_l^m(\cos\theta)\right\} \qquad (3)$$

is a spherical harmonic series having $(L+1)^2$ "shape parameters" a_{lm}, b_{lm} (4). The surface S of a two-component model is the union of the surfaces of two one-component models: $S = S_1 \cup S_2$, where $S_i = \{\mathbf{r}\,|\mathbf{r} = \mathbf{r}_i - \mathbf{r}_{0i}\}$ and $r_i = r_i(\theta,\phi)[\sin\theta\cos\phi, \sin\theta\sin\phi, \cos\theta]$ for i = 1,2. The radius functions $r_1(\theta,\phi)$ and $r_2(\theta,\phi)$ each have their own spherical harmonic series, and r_{o1} and r_{o2} are the corresponding centers of the individual components.

We modeled the delay-Doppler data set as

$$\sigma_m(\tau,\nu;\psi) = \iint I(\mathbf{r})h_\tau[\tau - \tau(\mathbf{r})]h_\nu[\nu - \nu(\mathbf{r})]\sigma_0(\mathbf{r})\,dS\ . \qquad (4)$$

Here $I(\mathbf{r})$ is unity if the point r is illuminated by the radar or zero otherwise, and h_τ and h_ν are the time and frequency impulse-response functions. The angular scattering law $\sigma_0(\mathbf{r})$, defined so $\sigma_0(\mathbf{r})\,dS$ is the radar cross section of a surface element dS at r, is assumed to have the form:

$$\sigma_0(\mathbf{r}) = \rho\cos^n i(r)\ , \qquad (5)$$

● R. S. Hudson is at the School of Electrical Engineering and Computer Science, Washington State University, Pullman, WA 99164-2752. S. J. Ostro is at 300-233, Jet Propulsion Laboratory, Pasadena, CA 91109-8099.

where i(r) is the angle of incidence, n measures the specularity of the surface, and ρ describes the radar brightness of the surface at normal incidence (i = O). In addition we used: 64 factors to permit recalibration of each frame'sb rightness scale, which had relied on an empirical function describing the sensitivity of the Arecibo telescope, 64 delay-registration parameters to compensate for small, random, frame-to-frame shifts in the sampling time base, and a frequency offset to correct the a priori Doppler ephemeris.

The accuracy of any shape model derived from the Castalia data is limited by the fact that only one subradar latitude is sampled. If our view were too close to equatorial ($\delta \sim 0°$) the reconstruction would be north/south ambiguous, whereas if $|\delta|$ were at least a few tens of degrees (as appears to be the case here), then the rotational phase coverage would provide sufficient geometric leverage to overcome N/S ambiguities (5), but the polar region opposite the radar-facing pole would have been unseen and hence poorly constrained. More generally, the data might support relatively high-resolution (large-L) reconstruction of some regions of the surface (where the backscattering is strong or which contribute to many frames) but not in others. We have chosen to use the highest-resolution (largest-L) model we felt was both computationally practical and adequate to ensure reliable reconstruction of well-imaged regions, and then to use penalty functions, described below, to suppress surface features that do not seem to be required by the observations. We settled on L = 12, or 169 shape parameters, for the one-component model and L = 8, or $2(8 + 1)^2 + 5 = 167$ shape parameters, for the twc-component model (6). The total numbers of free parameters in the one- and two-component models were 300 and 298, respectively.

Because parts of the asteroid are not well constrained by the observations, we cannot test hypotheses that involve the object's internal density distribution or rotational stability. To ensure plausible extrapolation of the reconstructed surface into unconstrained regions, we assumed uniform density and principal-axis rotation.

We treated the reconstruction process by minimizing an objective function $\Phi(\mathbf{p})$ using Powell's method (?) to estimate the free parameters p. We took

$$\Phi(\mathbf{p}) = \chi^2(\mathbf{p}) + 10^{\beta_A} A(\mathbf{p}) + 10^{\beta_B} B(\mathbf{p}) + 10^{\beta_C} C(\mathbf{p}) + 10^{\beta_D} D(\mathbf{p}), \quad (6)$$

where

$$X2(P) = \sum_{\tau\nu\psi} [\sigma_m(\tau, \nu; \psi) - \sigma(\tau, \nu; \psi)]^2 / s^2_{\tau\nu\psi} \quad (7)$$

describes the goodness-of-flt between observed and modeled data. The variance $s^2_{\tau\nu\psi}$ of pixel $\tau\nu\psi$ includes contributions from receiver noise and echo self noise.

The "penalty functions" *A(p),* **B(p), C(p), D(p) are defined** as follows. *A(p) is* the square of the distance between the model's centroid and its spin axis. $B(\mathbf{p})$ is the square of the sine of the angle γ between the spin axis and the model's principle axis of the greatest inertia, Making β_A and β_B large forces A(p) and $B(\mathbf{p})$ to be small, producing a dynamically plausible model under the assumption of uniform density. $C(\mathbf{p})$ is a concavity penalty given by $C(\mathbf{p}) = \iint U[\kappa_m(\mathbf{r})]\kappa_m^2(\mathbf{r})\, dS$ with U the unit step function and $\kappa_m(\mathbf{r})$ the maximum surface curvature (8) at point $\mathbf{r}$. Since $K_m(r) > 0$ at a concavity, the integral is zero for a convex model, exceeds zero if any concavities exist, and increases as concavities become more prominent. D(p), a proximity penalty applicable only to two-component models, is the reciprocal of the distance between the components' centroids. Increasing β_C suppresses concavities, and increasing β_D forces the two components apart.

We obtained approximate values for the non-shape parameters from a biaxial ellipsoid fit to the data, used them to initialize the one-component model, and then sought a least-squares solution for the full parameter vector. The penalty factors β_A and β_B were set large enough to keep γ from exceeding a few degrees and to keep the centroid within a few tens of meters of the spin axis, and the concavity penalty factor β_C was set low enough to avoid any noticeable effect on the fits. This process yielded frame-to-frame calibration corrections of order 10% and delay registration corrections of order 0.5 μs, in each case consistent with a priori expectations about the performance of the Arecibo radar system (9). As an example of the model's sensitivity to a non-shape parameter, Fig. l(A) plots postfit χ^2 vs. values of the subradar latitude $|\delta|$ at 5° intervals.

The one-component estimations yielded distinctly non-ellipsoidal shapes with a variety of concavities, notably a crevice, or waist, that encircles the middle of the body and is roughly perpendicular to the body's longest dimension. Figures 1(B) and 2(A) show how χ^2 and the model's shape depend on the concavity penalty factor β_C, that is, on how strongly concavities are penalized. Penalizing concavities by increasing β_C to 5 almost eliminates the waist, but causes a severe increase in X^2. We conclude that the waist is required to fit the data; Castalia is distinctly bifurcated into two lobes. We take the β_C = 4, one-component model to represent a lower bound on the asteroid's bifurcation.

To place an upper bound on the severity of the bifurcation, we used a two-component model and studied the dependence of shape and χ^2 on the proximity penalty factor β_D. The two-component parameter set and the penalty factors (β_A, β_B, β_C) were initialized with values from the β_C = 4 one-cornponent model. However, here the concavity penalty function C(p) was defined as the sum of integrals for each component, so it received no contribution from the waist, whose evolution was then independent of β_C (10). Figures 1(C) and 2(B) show how χ^2 and the shape depend on β_D, i.e., on how strongly the component centroids are forced apart. At $\beta_D = 6$ the components are barely in contact, but χ^2 has increased dramatically. We conclude that substantial contact between the components is required to explain the data and we take the β_D = 5.4, two-component model to represent an upper bound on the severity of Castalia's bifurcation.

We adopt the β_D = 4, two-component model as a nominal working model of the asteroid, The root-reduced-chi-square goodness-of-fit statistic, RRC = $[\chi^2/(N_d - N_p)]^{1/2}$, with N_d = 5824 the number of observed data and N_p = 298 the number of free parameters, calculated over 2-km by 2-km frames, is 1.5. This value of RRC might be interpreted to mean that the modeling is incomplete (e.g., L may be too small) or inaccurate (e.g., the assumed scattering law may be simplistic). However, the formal probabilistic interpreta-

tion of this statistic in linear lead-squares estimation is not applicable here, because of extreme nonlinearity of the mathematical model and also because of the difficulty of quantifying the effective increase in the number of degrees of freedom $(N_d - N_p)$ that is caused by use of the penalty functions, especially C(p) and D(p) (*11*).

Nonetheless, we were concerned that our assumption of a uniform scattering law (Eqn. 5) may have been overly restrictive. To test for the presence of variations in reflectivity ρ and specularity n, we explored one-component models that allowed both parameters to be functions of surface location, by expanding each in its own L = 8 spherical harmonic. series. The estimation, which involved 160 ncw parameters, did not reduce RRC and hence fails to offer compelling evidence for heterogeneity in the radar properties of Castalia's surface. Large-scale (> 100-m) variations in near-surface bulk density or roughness therefore seem unlikely (*12*).

Our reconstruction shows Castalia to be a strongly bifurcated body whose convex hull has maximum dimensions 0.7 x 1.0 x 1.6 km (Figs. 3, 4). The asteroid's prominent waist has a typical depth between 100 and 150 m with respect to the object's convex hull. The depth and sharpness of the waist support the hypothesis (9) that at one time the lobes were separate and that the current "contact-binary" configuration resulted from a relative] y gentle collision.

Our Castalia model is distinctly nonconvex and nonellipsoidal. Its volume (0.68 km^3) is 10% less than that of its convex hull and its rms radial deviation from that hull (averaged over all θ, ϕ and normalized to the model's mean radius of 0.50 km) is $\Delta r_{hull} = 10\%$. The model's deviation from its best triaxial-ellipsoidal approximation, $\Delta r_{ell} = 14\%$, exceeds the corresponding value, 11%, for the mainbelt asteroid 951 Gaspra (*13*) which deviates more from an ellipsoid than Phobos, Deimos, any other planetary satellite observed by spacecraft or any asteroid for which stellar-occultation limb profiles arc available (14). Therefore Castalia, the smallest planetary object imaged so far, is also the most irregularly shaped. The individual lobes, labeled alpha and beta in Fig. 4, have mean radii equal to 0.46 and 0.40 km and Δr_{ell} equal to 11% and 12%.

The only fundamental limitations on the resolution of a shape reconstruction from radar images are the delay-I)opplcr resolution, orientational coverage, and signal-to-noise ratio of those images. At present, the Arecibo and Goldstone radars can achieve resolution an order of magnitude finer than that of the Castalia data. By 1995, compaction of instrumentation upgrades now underway should allow useful imaging and reconstruction of several of the currently known ECAs pcr year.

REFERENCES AND NOTES

1. The apparent spin vector ω at any time t is the sum of the intrinsic (sidereal) spin vector ω_s and the contribution $\omega_o = (d\mathbf{e}/dt) \times \mathbf{e}$ arising from the changing direction of the target-t o-radar unit vector $\mathbf{e}$.

2. S. Hudson, *Remote Sensing Reviews* 8, 195 (1993).

3. S. J. Ostro et rd., Science 248, 1523 (1990).

4. T. Duxbury, *Icarus* 78, 119 (1989), outlined merits and drawbacks of the use of spherical harmonics to model irregularly shaped solar system objects. He fit a one-component model with $L = 6$ (i.e., 49 shape parameters) to spacecraft images of Phobos.

5. Echoes from N/S ambiguous points can, in principle, be distinguished if 6 # O, because they execute different delay-Doppler trajectories as the target rotates.

6. Five parameters are needed to described the locations of the components' centers relative to each other and to the spin vector.

i'. W. 11. Press, B. P. Flannery, S. A. Teukolsky, W. T. Vetterling, Numerical *Recipes in C*, (Cambridge Univ., Cambridge, 1988).

8. D. J. Struik, *Lectures* on *Classical Differential Geometry* (Dover, New York, ed. 2, 1988).

9. Estimates of nonshape parameters include an independent value for the rotation period ($P = 4.07 \pm 0.03$h) and refined values for the time delay τ and 2380-MHz Doppler frequency ν of hypothetical echoes from Castalia's center of mass, received at the center of curvature of the Arecibo telescope's main reflector, at the epoch 1989 Aug. 22, 06:45:00 UTC: $\tau = 37{,}453{,}006.9 \pm 0.3\mu$s, $\nu = 173{,}116.5$* 0.1 HZ.

10. The Castalia data apparently require a waist with severe surface curvature. The rippled appearance of the low-β_C, one-component models in Fig. 2 (A) is an artifact, called Gibbs' phenomenon, of trying to use a truncated series to represent a sharply curving, nearly discontinuous function. The two-component model avoids this drawback.

11. Removing the "dynamical" penalty functions A(p) and B(p) and allowing the nominal model to reconverge decreased χ^2 by less than 0.1%.

12! For the nominal model, estimates of the scattering-law exponent and reflectivity (see Eqn. 5) are: $n = 2.8 \pm 0.3$, $p = 0.30 \pm 0.03$, where the uncertainties encompass values for the upper- and lower-bound models. The most commonl y used measure of a radar target's reflectivity is the radar albedo $\hat{\sigma} = \sigma / A_p$, i.e., the target's radar cross section divided by its pro jetted area. Cast alia's model albedo, averaged over all 64 frames, is 0.12 ± 0.01. A sphere with Castalia's values for p and n would have a radar albedo $\hat{\sigma} = 2\rho/(n+1) = 0.1\,\mathrm{G} \pm 0.01$; this "equivalent spherical al bedo" may permit more useful comparisons with other radar targets.

13. M. J. S. Belton *et* al., Science 257, 1647 (1992),

14. P. C. Thomas, *Icarus* 77, 248 (1989).

15. For a single-date observation, if 6 is replaced by -6 and the model is replaced by its mirror image through the equatorial plane, then the modeled delay-Doppler data is unchanged, The spin vector's sign (i.e., the sense of rotation) and its azimuthal coordinate could have been constrained if other radar-target directions had been sampled.

16. This research was conducted at Washington State University and the Jet Propulsion Laboratory, California Institute of Technology, under contract with the National Aeronautics and Space Administration (NASA).

FIGURE CAPTIONS

1. (A) Percentage increase of X^2 over its minimum value as a function of subradar latitude $|\delta|$ for estimations using the one-component model. The least-squares estimate, 35°, defines the locus of possible pole directions as a cone with axis parallel to the radar line of sight (right ascension = 0.30 h, declination = 25.4°) and interior half angle 55° (*15*). Shape models for $|\delta|$ equal to 30° and 40° look similar to that for $|\delta|$ = 35°, whereas the respective models for 25° and 45° are noticeably smaller and larger. The inverse correlation between size and $|\delta|$ stems from Eqn. 1, and the increase in χ^2 away from 35° reflects the pressure that the echoes' delay dispersion exerts on estimation of the model's size. Based on our understanding of these results and numerous simulations, we assign an intentionally conservative standard error of ±10° to our estimate of $|\delta|$. (B) Percentage increase of χ^2 over its minimum value as a function of the concavity penalty factor β_C for estimations with the one-component model. (C) Percentage increase of χ^2 over its minimum value as a function of the proximity penalty factor β_D for estimations with the two-component model.

2. (A) Plane-of-sky views of models corresponding to β_C = 3.0,4.0,4.5,5.0. Views are at subradar latitude 6 = 35" and rotation phases of $\psi \sim$ 53° (top row) and $\psi \sim$ 157° (bottom row), corresponding to frames 16 and 45 in Fig. 3 of (*3*). Models are rendered with a Lambertian (n = 2) scattering law, χ^2 is essentially insensitive to $\beta_C \leq 3$, has increased by 2% at β_C = 4, and rises steeply thereafter. Much bumpiness is smoothed out as we raise β_C from 3 to 4, but the waist remains intact. We take the β_C = 4 model to represent a lower bound on Castalia's bifurcation. (B) Plane-of-sky views of models corresponding to β_D = 5.0,5.4,5.8,6.0. Orientations and scattering law are the same as in (A). χ^2 is essentially insensitive to $\beta_D \leq$ 5, has increased by *2%* at β_D = 5,4, and rises steeply thereafter. We take the β_D = 5.4 model to represent an upper bound on Castalia's bifurcation.

3. Plane-of-sky views of the nominal model of Castalia at subradar latitude 6 = 35° and rotation phases ψ = 0° to 220° in steps of 20°. Lobe alpha (see Fig. 4) is between the viewer and lobe beta at ψ = 60°, The Lambertian scattering law used for this rendering and in Fig. 2 is somewhat less specular than the radar scattering law estimated in our reconstruction and much more specular than optical scattering laws thought to characterize asteroids.

4. Perspectives showing projections of the nominal Castalia model (thick solid curve), the lower-bound model (dashed curve), and the upper-bound model (thin solid curve). (A) Pole-on view of model silhouettes. The spin axis is denoted by the dot in lobe alpha. Arrows radiating from that dot point toward the radar at rotational phases ψ = 0°,60°, 150°, and 220°; the radar data $\sigma(\tau, \nu; \psi)$ cover phases from 0° to 220°. (B) 'Broadside" view from within the equatorial plane at ψ = 150°. (C) 'End-on" views from within the equatorial plane at ψ = 60°. (D) Cross-sections corresponding to the dotted-line slice through the pole-on view. The dotted vertical lines in (B), (C), and (D) represent the spin axis. Each quadrant is a 2 x 2 km square and the tic marks are at 0.2-km intervals. The curve defined by the intersection of the two lobes in the nominal model is nonplanar. 'I'he rms deviation of that curve from its best-fit plane is 0.16 km. That plane lies 0,17 km from the nominal model's center of mass along a line that points towards (ψ, δ) = (241°, 80).

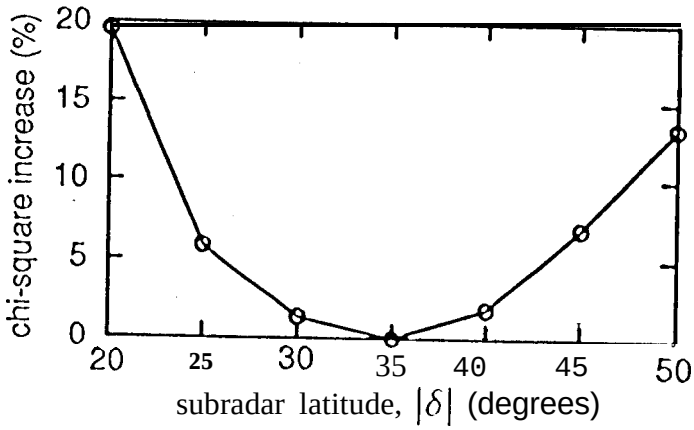
chi-square increase (%)
20
15
10
5
0
20
25
30
35
40
45
50
subradar latitude, $|\delta|$ (degrees)

A

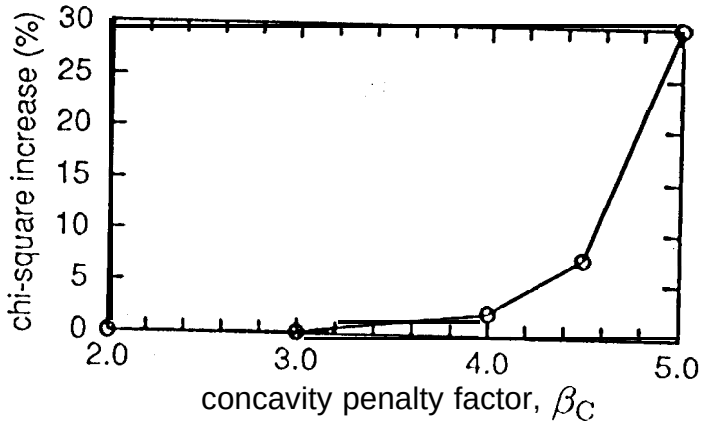
chi-square increase (%)
30
25
20
15
10
5
0
2.0
3.0
4.0
5.0
concavity penalty factor, β_C

B

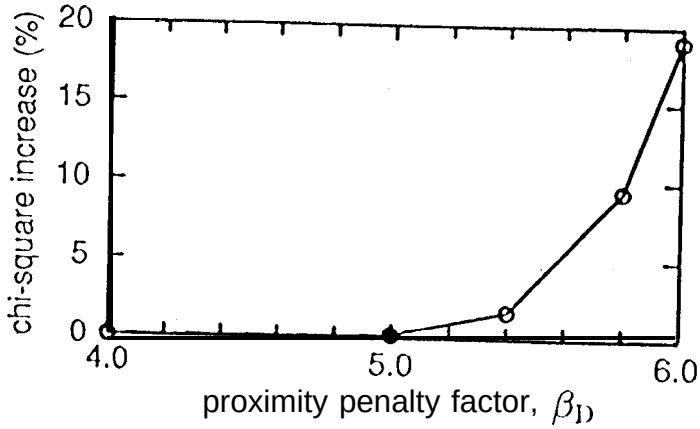
chi-square increase (%)
20
15
10
5
0
4.0
5.0
6.0
proximity penalty factor, β_D

C

FIG. 1

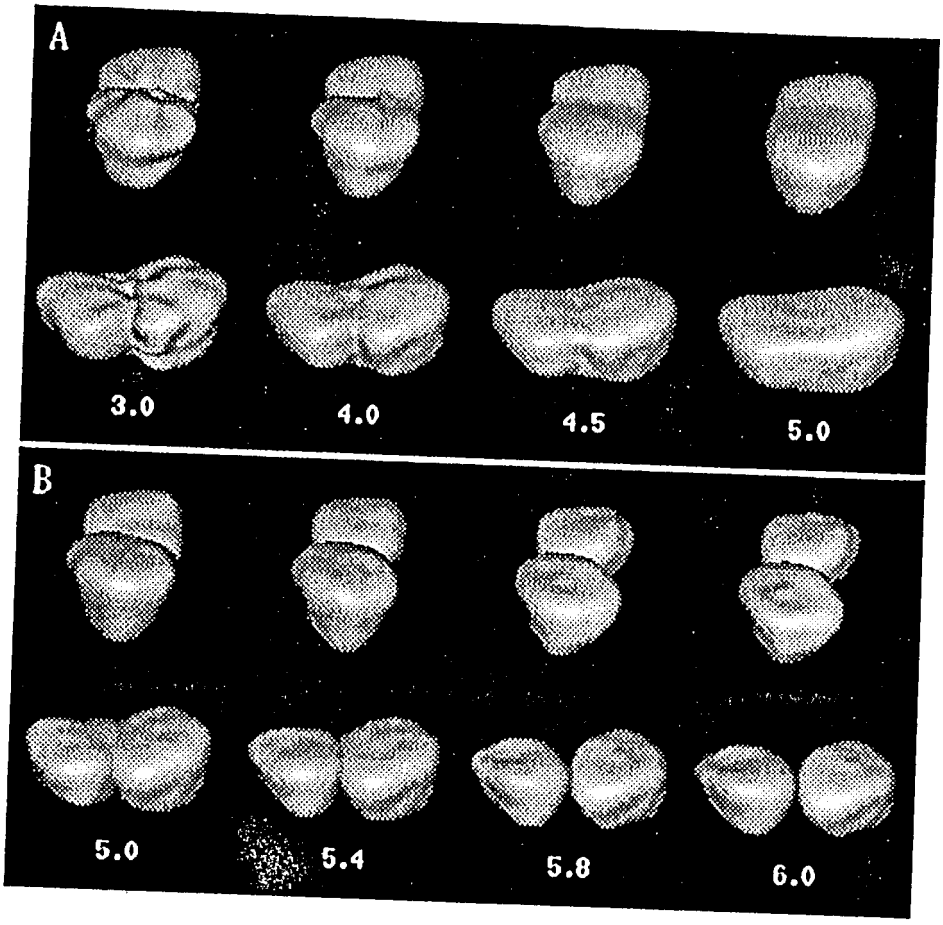

FIG. 2

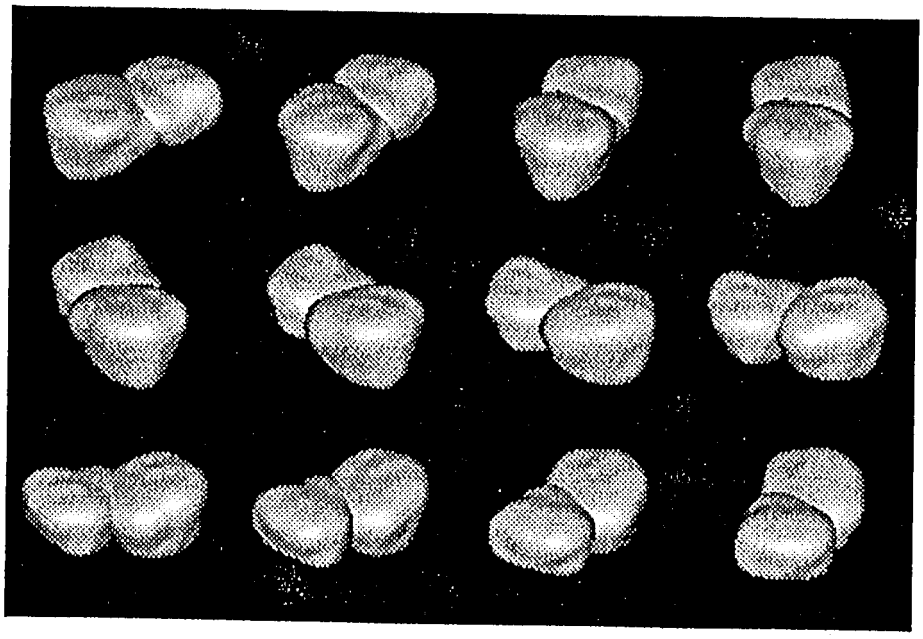

FIG. 3

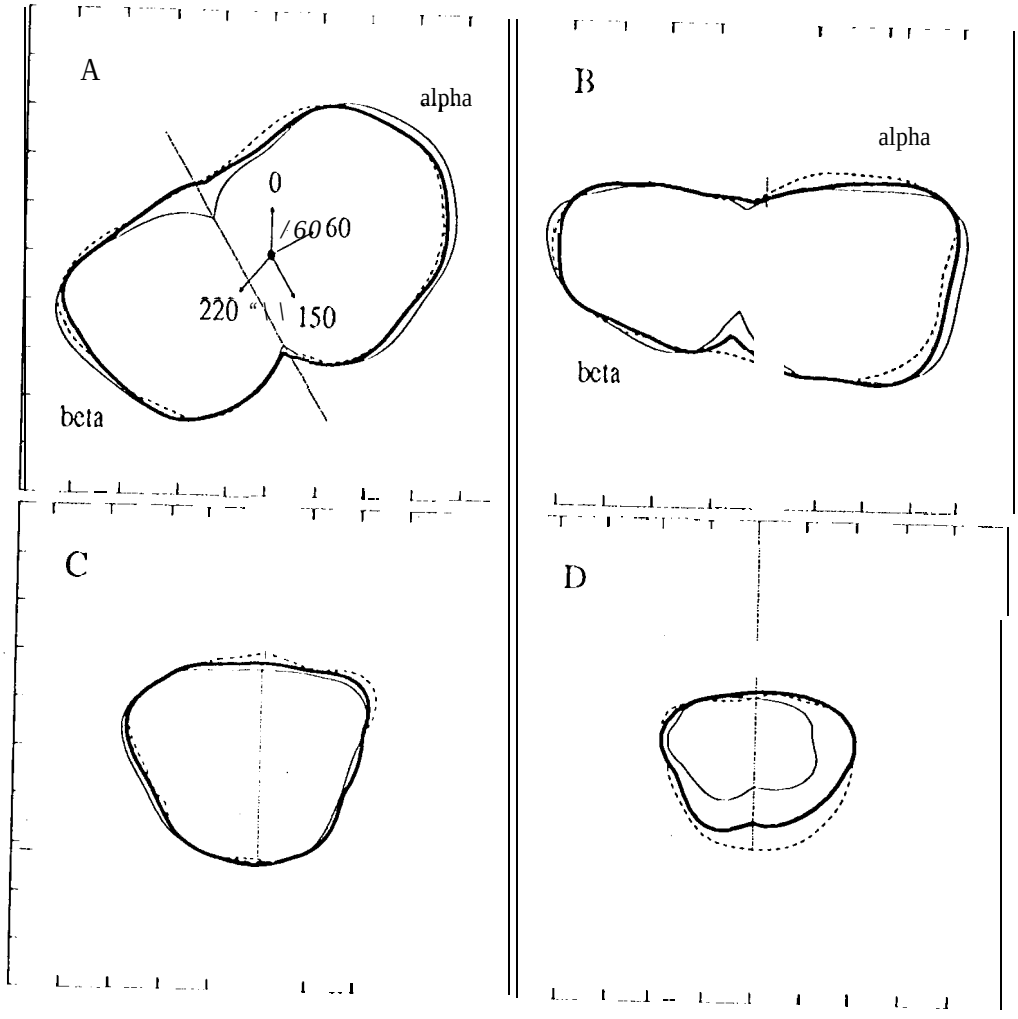

FIG. 4